

# **An efficient strategy to construct general machine learning potentials for high-entropy ceramics**

Yiwen Liu, Hong Meng, Zijie Zhu, Hulei Yu\*, Lei Zhuang, Yanhui Chu\*

School of Materials Science and Engineering, South China University of Technology,

Guangzhou, 510641, China

---

\* Corresponding author.  
*E-mail address:* [huleiyu@scut.edu.cn](mailto:huleiyu@scut.edu.cn) (H. Yu); [chuyh@scut.edu.cn](mailto:chuyh@scut.edu.cn) (Y. Chu)

## **Abstract**

Molecular dynamics (MD) simulations are considered an efficient and low-cost means to develop remarkable properties of high-entropy ceramics with vast composition space, yet the lack of general potentials severely limits their applications. Herein, taking high-entropy carbides (HECs) as the model, we propose a strategy to efficiently construct a general neuroevolution potential (NEP) with broad compositional applicability for HECs. Specifically, the small dataset comprising unary and binary carbides with ten transition metal principal elements is first identified as the most efficient choice to train the general NEP for HECs, and then a highly accurate and transferable NEP is constructed. Further MD predictions on structural, mechanical, and thermal properties of HECs using the established NEP show good agreement with the results of first-principles calculations and experimental measurements, validating the accuracy, generalization, and reliability of our developed NEP. Our work provides an efficient solution to accelerating the MD simulations searching for high-entropy ceramics with desirable properties.

**Keywords:** High-entropy ceramics, machine learning potentials, first-principles calculations, molecular dynamics.

## 1. Introduction

High-entropy ceramics, a class of emergent multicomponent materials with four or more principal elements, have attracted substantial attention in the ceramic community since they were first proposed in 2015 [1-4]. Owing to their compositional complexity and unique microstructures, high-entropy ceramics have been shown to possess a range of superior properties exceeding those of their individual component ceramics, such as better thermal stability [1,2,5,6], enhanced mechanical properties [3,4], exceptional oxidation and ablation resistance [7-10], higher catalytic activity [11,12], improved thermoelectricity [13-14], and remarkable superionic conductivity [15]. These distinctive characteristics have made them great potential for various structural applications [3-10], such as hypersonic thermal protection systems and high-speed cutting tools, as well as functional applications[11-15], like catalysts, thermoelectrics, and electrodes. Nevertheless, research on the properties of high-entropy ceramics is still in the early stages, failing to meet the growing demand from future structural and functional application domains. Therefore, it is imperative to develop high-entropy ceramics with desired properties.

Due to the large composition space, the experimental approach to searching for high-entropy ceramics with desirable characteristics is both time-consuming and costly. To this end, molecular dynamics (MD) simulations, which have been extensively applied in high-entropy alloys (HEAs) [16-18], have emerged as an effective and powerful solution. However, conventional interatomic potentials for high-entropy ceramic systems are either absent or inapplicable with low accuracy, making their MD

simulations inaccessible. To address this issue, machine learning potentials (MLPs), as a frontier data-driven approach, have been developed to achieve quantum-level accuracy of first-principles calculations while maintain computational efficiency comparable to empirical potentials [19-21]. To date, MLPs have been successfully adopted in various ceramics, like  $\text{TiO}_2$  [22],  $\text{Ti}_3\text{O}_5$  [23], and  $\text{TiB}_2$  [24], whereas the applications of MLPs in high-entropy ceramics are seldom reported, with only two attempts proposed by Dai et al. on constructing MLPs for  $(\text{Ti}_{0.2}\text{Zr}_{0.2}\text{Hf}_{0.2}\text{Nb}_{0.2}\text{Ta}_{0.2})\text{B}_2$  [25] and  $(\text{Zr}_{0.2}\text{Hf}_{0.2}\text{Ti}_{0.2}\text{Nb}_{0.2}\text{Ta}_{0.2})\text{C}$  [26]. The dominant constraint lies in the poor transferability of the trained MLP with the conventional construction strategy, where the MLP is trained from a fixed-composition dataset. Therefore, there is an urgent need to build general MLPs with broad compositional applicability, enabling the effective and economical development of high-entropy materials with desired properties. Recent studies have demonstrated improved transferability in MLPs trained with varied compositions in HEAs, promoting MD simulations on their plasticity and primary radiation damage performance [28]. However, there is still a lack of efficient ways to construct accurate and transferable MLPs for high-entropy ceramics, significantly hindering the further exploitation of high-entropy ceramics with desired properties.

In this work, taking the high-entropy carbide (HEC) system as an example, we propose a strategy to efficiently build general neuroevolution potentials (NEPs) with high accuracy and transferability based on unary (1HEC; the carbides with  $n$  types of transition metal (TM) principal elements are notated as  $n\text{HECs}$ ) and binary (2HEC) carbide training data with up to ten TM elements (see **Fig. 1**). Various effects, including

the computational cost and modeling complexity of density functional theory (DFT) computations as well as accuracy and transferability of NEPs trained from different datasets, on the construction of NEPs are first discussed, and a combination of 1HEC and 2HEC (1+2HEC) configurations is identified as the optimal training dataset choice. The high transferability and accuracy of the established NEP are then assessed and verified by considering its applicability to HECs. Further predictions on the structural, mechanical, and thermal properties of HECs using MD simulations validate the accuracy, generalization, and reliability of the trained NEP for HECs. Our established NEP can efficiently accelerate the discovery of HECs with desired properties via MD simulations.

## 2. Experimental and computational methods

### 2.1 DFT calculations

All DFT calculations were implemented in the Vienna *ab initio* simulation package (VASP) with the projector augmented wave (PAW) [29,30]. The Perdew-Burke-Ernzerhof (PBE) under the generalized gradient approximation (GGA) was applied to approximate the electronic exchange and correlation function [31]. Supercells of 1-10HECs were built based on the ZrC conventional cell, and the special quasi-random structure (SQS) approach was performed in the Alloy Theoretic Automated Toolkit (ATAT) [32,33] for 2-10HECs. Detailed supercell sizes are summarized in **Table S1**. All the structures were fully relaxed initially to obtain the lattice constants. Additionally, elastic tensors from DFT were calculated using the energy-strain approach [34]. Voigt-

Reuss-Hill method was also used to evaluate the bulk modulus ( $B$ ) and the shear modulus ( $G$ ) of HECs [35].

For the *ab initio* molecular dynamics (AIMD) calculations [36], a plane-wave energy cutoff of 300 eV was used, and only the  $\Gamma$  point in the Brillouin zone was considered. A time step of 3 fs and a total simulation time of 6 ps were applied under the NPT ensemble. The simulated temperatures were set to 1000, 2000, 3000, and 4000 K, respectively. For accurate single-point calculations of configurations, the plane-wave cutoff energy was set to 450 eV, and the Brillouin zone was sampled employing the  $\Gamma$ -centered method with a separation of approximately  $0.5 \text{ \AA}^{-1}$  [37]. The energy convergence criterion of the electronic self-consistency cycle was set to  $10^{-5}$  eV.

## 2.2 NEP constructions

Small-scale 1HEC, 2HEC, 3HEC, and 1+2HEC (50% 1HEC and 50% 2HEC) training datasets were first developed with each comprising 1000 configurations from AIMD calculations. The distribution of different TM elements in the datasets was ensured with the highest degree of equality. Based on these training datasets, state-of-the-art NEPs were then trained within the Graphics Processing Units Molecular Dynamics (GPUMD) code [38]. The detailed training hyperparameters are listed in **Table S2**. In addition, a corresponding testing dataset with 1-10HECs was constructed by a total of 300 randomly selected configurations (30 configurations for each  $n$ HEC) to evaluate the performance of the trained NEPs from these small-scale training datasets.

A large 1+2HEC training dataset containing 55 kinds of chemical compositions and 5500 configurations (100 configurations for each composition collected from

AIMD) was built to train the accurate NEP for HECs. Meanwhile, 1500 configurations of randomly picked 71 kinds of HECs (ten kinds of chemical compositions each from 3-9HECs and the unique composition from 10HEC) were collected to build the 3-10HEC testing dataset with the best assurance of equally distributed TM elements. 20 configurations in each of the 3-9HEC compositions and 100 configurations in the 10HEC composition were selected from AIMD at the abovementioned four temperatures for static calculations.

### **2.3 Molecular dynamics simulations**

The Large Scale Atomic/Molecular Massively Parallel Simulator (LAMMPS) package was utilized to perform MD simulations interfaced with the NEP code [39]. All the simulated models were built by randomizing the TM elements in a  $20 \times 20 \times 20$  FCC supercell (a total of 64000 atoms). A time step of 1 fs was maintained throughout the simulations. Periodic boundary conditions were used in all directions. All models were first equilibrated using the NVT ensemble for a period of 10 ps, and then relaxed using the NPT ensemble for a period of 10 ps, and finally equilibrated using the NVT ensemble for a period of 10 ps at 300 K. Elastic tensors from MD were then calculated by deforming the simulation box with the strain-stress methods at zero temperature. Equilibrium lattice constants from 300 K to 1000 K with an interval of 100 K were obtained to evaluate the coefficients of thermal expansion (CTEs). For the previously reported CTEs, temperature ranges were adjusted according to experimental conditions. The melting point was simulated by first equilibrating at 2000 K for 100 ps using the NVT ensemble before being elevated to 4000 K with a heating rate of 5 K/ps using the

NPT ensemble. The thermal conductivity was predicted by using the GPUMD package through the equilibrium molecular dynamics (EMD) method [38] with a timestep of 1 fs and periodic boundary conditions. All models were equilibrated for 20 ps using the NPT ensemble with a target temperature of 300 K before collecting the following 1 ns heat current data in the NVE ensemble.

## 2.4 Experimental methods

The high-quality  $(\text{Ta}_{1/4}\text{Nb}_{1/4}\text{Ti}_{1/4}\text{Zr}_{1/4})\text{C}$ ,  $(\text{Ta}_{1/6}\text{Nb}_{1/6}\text{Ti}_{1/6}\text{Zr}_{1/6}\text{Hf}_{1/6}\text{Mo}_{1/6})\text{C}$ ,  $(\text{Ta}_{1/8}\text{Nb}_{1/8}\text{Ti}_{1/8}\text{Zr}_{1/8}\text{Hf}_{1/8}\text{Mo}_{1/8}\text{V}_{1/8}\text{W}_{1/8})\text{C}$  samples were fabricated via a two-step strategy involving ultrafast high-temperature synthesis and hot-press sintering techniques. The detailed synthesis process can be found in our previous work [40]. The CTEs of the samples (13.5 mm × 3 mm × 3 mm) were measured over the temperature range of 373-998 K at a heating rate of 5 K/min in a nitrogen atmosphere by a high-temperature dilatometer (Netzsch DIL 402C, NETZSCH, Selb, Germany). The referenced temperature for calculating CTEs was 298 K. The thermal diffusivity ( $h$ ) was measured at room temperature under an argon flow by a laser-flash apparatus (Netzsch LFA 427, Netzsch, Selb, Germany). The thermal conductivity ( $k$ ) of the samples was evaluated according to the following equation [41]:

$$k = h \cdot \rho \cdot C_p \quad (1)$$

where  $C_p$  is the specific heat capacity estimated based on the Dulong-Petit law and  $\rho$  is the density of the samples measured by the Archimedes drainage method. As the densities of all samples were almost the same as theoretical densities, no correction on  $k$  was considered.

### 3. Results and discussion

Unlike HEAs, where the metal principal elements are closely packed together, the metal principal elements in high-entropy ceramics are always separated by non-metal elements. As can be seen from Fig. 1, the first-nearest-neighbor atoms of TM atoms in carbides are all carbon atoms, forming an octahedron with TM-C bonding. This simple atomic environment can be perpetuated in HEC systems, which is beneficial to the construction of MLP descriptors for different HECs [19]. This indicates the possible applicability of MLPs between training datasets of carbides and their solid solutions. Based on these findings, it is anticipated that transferable MLPs applicable to various  $n$ HECs can be efficiently yielded from the training datasets comprising configurations of limited types of  $n$ HECs.

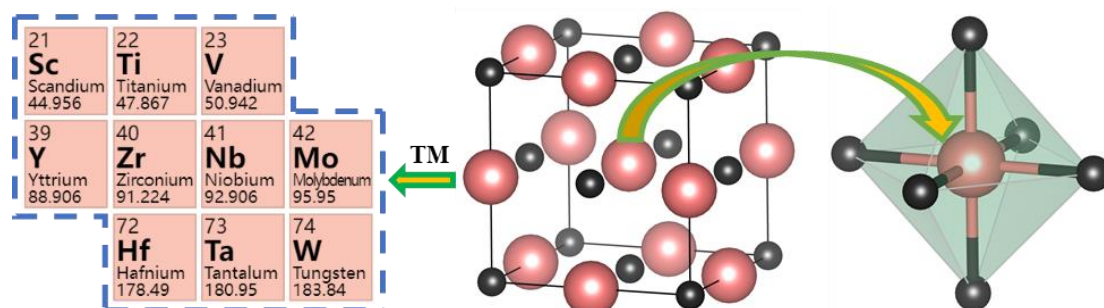


**Figure 1** Schematic of the crystal structure and the polyhedral of TM carbides. TM and carbon atoms are colored in pink and black, respectively.

To verify this hypothesis, the cost of building datasets and the performance of trained NEPs from different datasets were first investigated. In HECs, the number of TM elements has a significant influence on geometric modeling, resulting in different efficiencies in DFT calculations for each composition. As shown in **Fig. 2(a)**, it is found

that the elapsed times show an overall increasing trend from 1HECs to 10HECs, indicating an unfavorable efficiency in building training datasets with more TM elements in HECs. This can also be explained by the relatively lower symmetry in HECs with more TM elements. As 1-3HEC configurations have the highest computational speeds, NEPs are trained based on small-scale training datasets of 1HEC, 2HEC, 3HEC, and 1+2HEC, respectively, and their performances are presented in **Fig. S1-4** and Fig. 1(b). While the trained NEPs all possess high training accuracy with comparable root mean square errors (RMSE) in energy (3.7-5.6 meV), force (245-292 meV/Å), and virial (28.2-38.8 meV/atom), their transferability to the 1-10HEC testing dataset is quite different. Among the three NEPs trained from 1HEC, 2HEC, or 3HEC in Fig. 2 (b), 2HEC has the best testing accuracy with the lowest RMSEs of both energy and force. Compared to the 2HEC, the NEP trained from the 1+2HEC dataset is found to possess a much lower RMSE of energy with a reduction of 39.5% besides the comparable RMSE of force, indicating the better accuracy and transferability of the NEP trained from the 1+2HEC training dataset. In general, ten TM elements can yield a total of 1023 equimolar compositions in 1-10HECs. For the 1+2HEC dataset, merely ten kinds of 1HECs and 45 kinds of 2HECs need to be taken into consideration, significantly simplifying the modeling processes for AIMD calculations. Therefore, the 1+2HEC dataset is determined to be the most efficient training dataset.

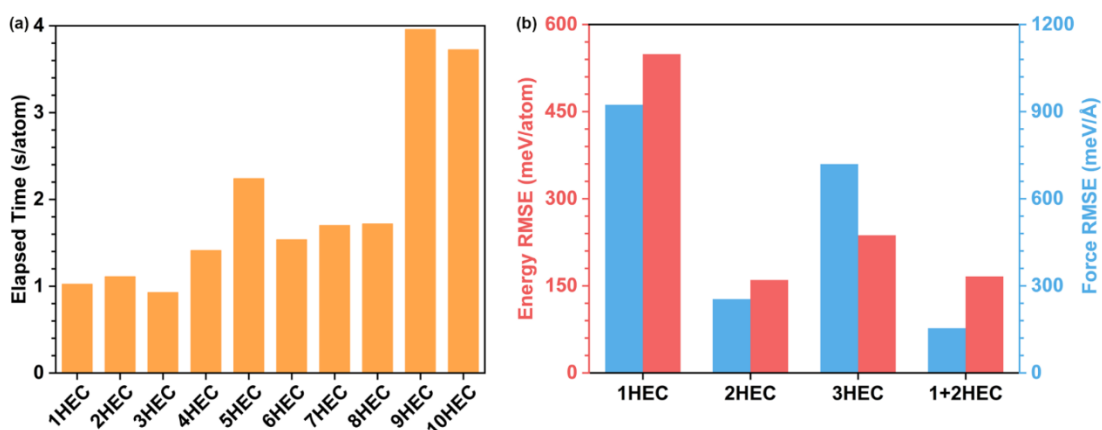


**Figure 2** Efficiency of DFT calculations and performance of NEP. (a) Average elapsed time of different HECs in DFT calculations. (b) Performance of NEPs with different training datasets (small-scale) to 1-10HEC testing datasets.

The accuracy of the trained NEP can be further improved by increasing the volume of the training dataset [21]. Here, a larger 1+2HEC training dataset, configurations increasing from 1000 to 5500, was built to construct the NEP with high accuracy. As shown in **Fig. 3(a)**, the L1 and L2 regularization loss functions show an increasing-then-decreasing trend over one million generations, indicating the effectiveness of the regularization. The loss of energy, force, and virial also converged, suggesting the well-trained NEP. In addition, the increase in the volume of the 1+2HEC training dataset has no significant influence on their training accuracy (see Fig. 3(b-d) and Fig S4). To examine the transferability of the trained NEP, a testing dataset based on 3-10HECs was built. As shown in Fig. 3(b-d), it is notable that the enlarged volume of the training dataset can greatly improve the testing accuracy, achieving low RMSEs of 15.7 meV, 301 meV/Å, and 49.1 meV/atom in energy, force, and virial, respectively. Although the accuracy of the trained NEP is promising to be optimized further by introducing more

training data (tens of thousands for most previous MLP works [22,26]), the present testing accuracies have already been sufficiently high for physical and chemical property explorations compared to previously reported MLPs [23,25,26,28], demonstrating the remarkable efficiency, transferability, and accuracy of our established NEP for HECs. Moreover, only a minor fluctuation in testing accuracies can be observed in individual testing accuracies of  $n$ HEC ( $n = 3\sim 10$ ) testing datasets from **Fig. S5**, indicating the generalization performance of our trained NEP to different HEC systems.

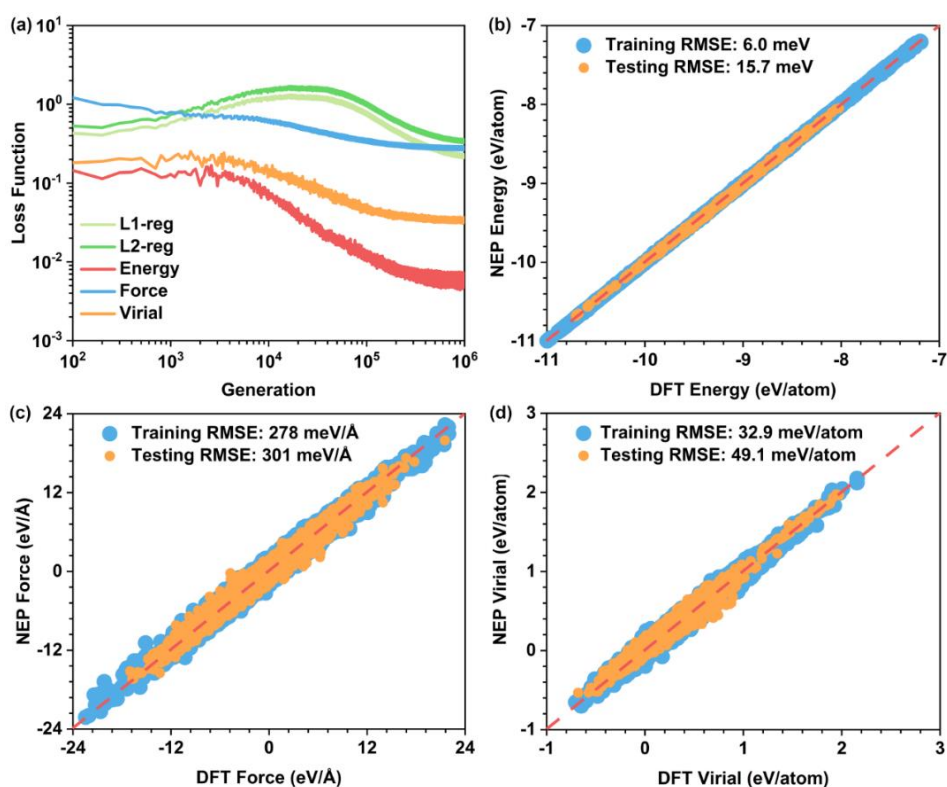


**Figure 3** Performance of the constructed NEP based on large-scale 1+2HEC training dataset. (a) Evolution of various loss functions with respect to generations. (b) Energy, (c) force, and (d) virial from NEP and DFT calculations for the 1-2HEC training dataset and the 3-10HEC testing dataset.

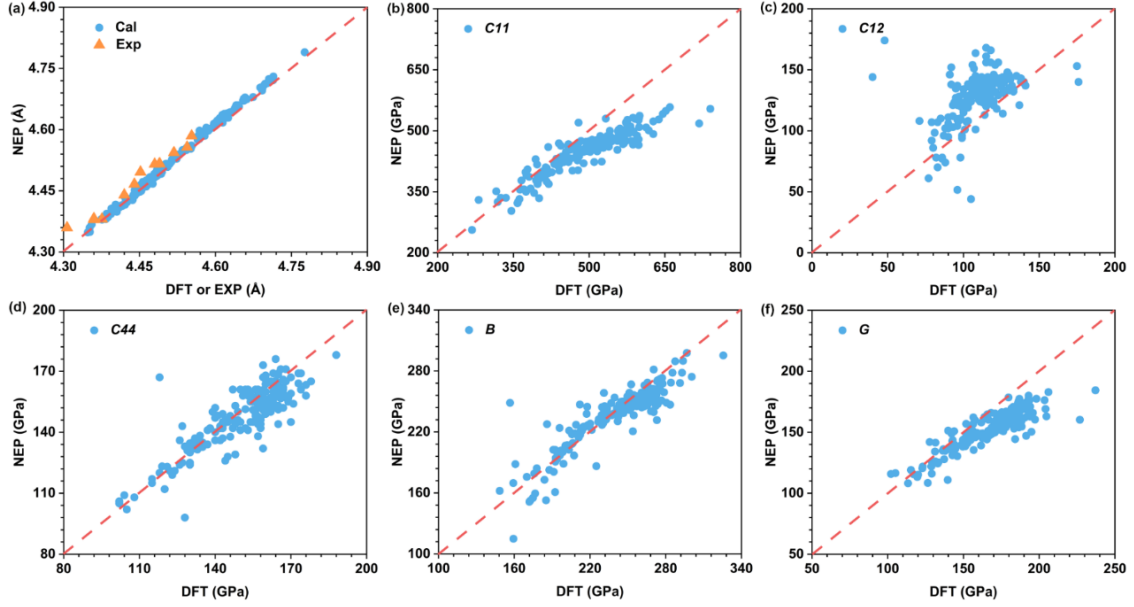


**Figure 4** Comparison of structural and mechanical properties of 4-10 HECs between NEP and DFT calculations. (a) Lattice constants. Experimental data are from Ref. [6,42-45]. (b-d) Elastic tensors  $c_{11}$ ,  $c_{12}$ , and  $c_{44}$ . (e) Bulk modulus. (f) Shear modulus.

To validate the reliability of our trained NEP, classic MD simulations with our trained NEP were carried out to predict lattice parameters ( $a$ ) and mechanical properties of HECs. A total of 200 compositions of different 4-10HECs are randomly selected. As displayed in **Fig. 4(a)**, the predicted  $a$  of 4-10HECs from MD simulations are well consistent with DFT results and reported experiments [6,42-45], indicating the reliability of the trained NEP. From Fig. 4(b-d), it can be found that the predicted three elastic constants ( $c_{11}$ ,  $c_{12}$ , and  $c_{44}$ ) of HECs are also comparable to those of DFT computations with the presence of small discrepancies. These differences are mainly attributed to the different model sizes and evaluation methods used for elastic tensors between MD and DFT calculations. Similar conclusions can also be drawn from  $B$  and  $G$  in Fig. 4(e,f), which exhibits a remarkable alignment between NEP and DFT

calculations. As a result, the established NEP has high accuracy and good generalization performance.

With the help of the trained NEP, CTEs of HECs are further predicted by MD simulations. **Fig. 5(a)** shows the calculated results and reported experimental values [46-56] of different 1HECs. Apart from VC, the theoretical results are in good agreement with experimental reports (within or almost within the bounds of experimental measurements), verifying the reliability of our predictions. The large discrepancy between our prediction and the reported experiment in VC may be attributed to its instability, where the face-centered cubic (FCC) VC phase is metastable from a thermodynamic perspective [57]. It should be mentioned that those 1HECs with large predicted CTEs, i.e., MoC, WC, YC, and ScC, are also energetically unstable in their FCC phases [57]. Moreover, the changes in the calculated CTEs of HECs are consistent with the ones from previous research [6,45,52] and our measurements, as listed in **Table 1**, further confirming the feasibility of our MD predictions for HECs. From Fig. 5(b), it is clear to see that CTEs of 4-10HECs are all located within the predicted CTE bound of 1HECs ( $7.04\text{-}20.5 \times 10^{-6}$  /K) with the maximum achieved in  $(\text{Ti}_{0.25}\text{V}_{0.25}\text{Sc}_{0.25}\text{Y}_{0.25})\text{C}$  ( $20.5 \times 10^{-6}$  /K) and the minimum in  $(\text{Ti}_{0.25}\text{Zr}_{0.25}\text{Hf}_{0.25}\text{Ta}_{0.25})\text{C}$  ( $7.52 \times 10^{-6}$  /K). It should be noted that, contrary to the high CTE predicted in the unstable ScC, the similarly high CTE in  $(\text{Ti}_{0.25}\text{V}_{0.25}\text{Sc}_{0.25}\text{Y}_{0.25})\text{C}$  is attainable due to the promising stability of  $(\text{Ti}_{0.25}\text{V}_{0.25}\text{Sc}_{0.25}\text{Y}_{0.25})\text{C}$  [58], suggesting the feasibility of searching exceptional performance in HECs with our NEP. Additionally, it can also be found from Fig. 5(b) that the rule of mixtures (ROM) method is found to have a

tendency to overestimate the CTEs of HECs compared to our MD simulations.

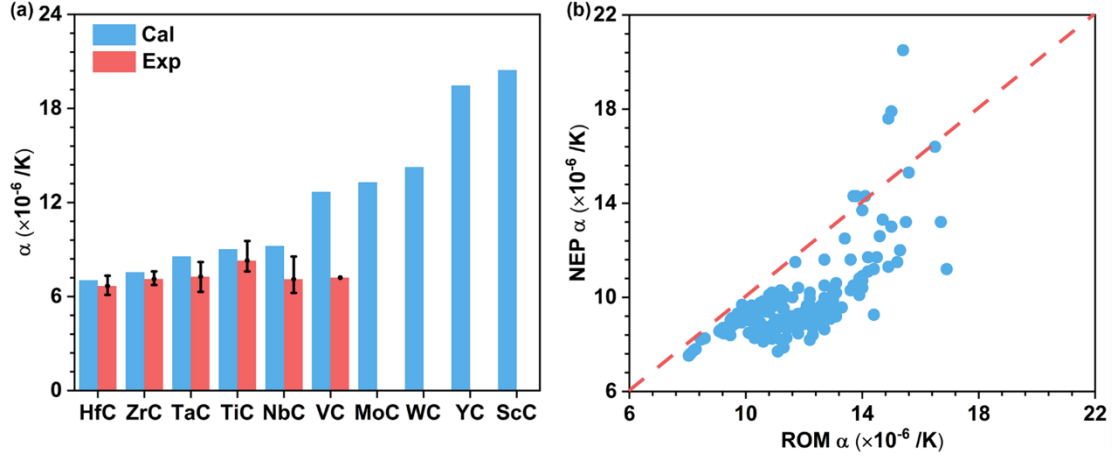


**Figure 5** CTEs of  $n$ HECs from NEP calculations, reported experiments, and ROM calculations. (a) CTEs of different 1HECs from NEP calculations and reported experiments [46-56]. Error bars are the maximum and minimum of the reported values. (b) CTEs of different 4-10HECs between NEP and ROM calculations.

**Table 1** CTEs of HECs from NEP calculations, reported literatures, and our measurements.

HECs	$T$ (K)	Exp ( $\times 10^{-6} / \text{K}$ )	Cal ( $\times 10^{-6} / \text{K}$ )
$(\text{Ti}_{1/5}\text{Zr}_{1/5}\text{Hf}_{1/5}\text{Nb}_{1/5}\text{Ta}_{1/5})\text{C}$	298-573	6.44 [6]	8.01
$(\text{Ta}_{1/4}\text{Nb}_{1/4}\text{Ti}_{1/4}\text{Zr}_{1/4})\text{C}$	298-998	7.05	8.24
$(\text{Ta}_{1/6}\text{Nb}_{1/6}\text{Ti}_{1/6}\text{Zr}_{1/6}\text{Hf}_{1/6}\text{Mo}_{1/6})\text{C}$	298-998	7.07	8.57
$(\text{Ti}_{1/5}\text{Ta}_{1/5}\text{V}_{1/5}\text{Mo}_{1/5}\text{W}_{1/5})\text{C}$	298-873	7.0-7.2 [45]	10.00
$(\text{Ti}_{1/5}\text{Zr}_{1/5}\text{Hf}_{1/5}\text{Ta}_{1/5}\text{W}_{1/5})\text{C}$	300-1200	7.7 (AIMD) [52]	8.49
$(\text{V}_{1/5}\text{Nb}_{1/5}\text{Ta}_{1/5}\text{Mo}_{1/5}\text{W}_{1/5})\text{C}$	300-1200	7.6 (AIMD) [52]	9.94

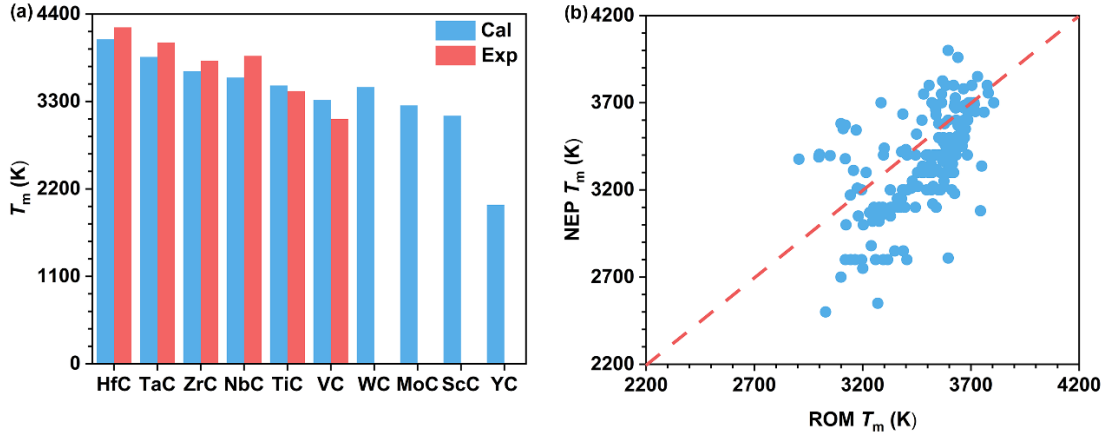


**Figure 6**  $T_m$  of  $n$ HECs from NEP calculations, reported experiments, and ROM calculations. (a)  $T_m$  of different 1HECs from NEP calculations and reported experiments [59-62]. (b)  $T_m$  of different 4-10HECs between NEP and ROM calculations.

**Table 2** Thermal conductivities of HECs from NEP calculations and our measurements.

HECs	Exp ( $\text{W}\cdot\text{m}^{-1}\cdot\text{K}^{-1}$ )	Cal ( $\text{W}\cdot\text{m}^{-1}\cdot\text{K}^{-1}$ )
$(\text{Ta}_{1/4}\text{Nb}_{1/4}\text{Ti}_{1/4}\text{Zr}_{1/4})\text{C}$	10.9	2.8
$(\text{Ta}_{1/6}\text{Nb}_{1/6}\text{Ti}_{1/6}\text{Zr}_{1/6}\text{Hf}_{1/6}\text{Mo}_{1/6})\text{C}$	5.5	2.0
$(\text{Ta}_{1/8}\text{Nb}_{1/8}\text{Ti}_{1/8}\text{Zr}_{1/8}\text{Hf}_{1/8}\text{Mo}_{1/8}\text{V}_{1/8}\text{W}_{1/8})\text{C}$	5.1	1.2

Since the melting points ( $T_m$ ) of carbides are generally over 3200 K [59-62], it is difficult to measure them directly in experiments. By utilizing MD computations with our trained NEP, the  $T_m$  of various HECs can be rapidly predicted. As shown in **Fig. 6(a)** and **Table S3**, the theoretical predictions for  $T_m$  of 1HEC are in good agreement with reported experiments [59-62] ( $\Delta \leq 8\%$ ), indicating the reliability of our trained

NEP. From Fig. 6(b), it can be observed that the predicted  $T_m$  of HECs are all within the bound of predicted  $T_m$  of carbides, where  $(\text{Ti}_{0.25}\text{Hf}_{0.25}\text{V}_{0.25}\text{W}_{0.25})\text{C}$  has the largest  $T_m$  (4000 K) among all the predicted 4-10HECs and  $(\text{Zr}_{0.25}\text{Hf}_{0.25}\text{V}_{0.25}\text{Y}_{0.25})\text{C}$  possesses the lowest  $T_m$  of 2550 K. Although the  $T_m$  prediction of ROM in Fig.6 (b) is improved compared to that in CTEs, it still tends to overestimate the values for 4-10HECs. In addition, the predictions on thermal conductivities of three selected HECs at 300 K were carried out. As listed in **Table 2**, it can be observed that there exists a reduction of experimental thermal conductivities from  $(\text{Ta}_{1/4}\text{Nb}_{1/4}\text{Ti}_{1/4}\text{Zr}_{1/4})\text{C}$  to  $(\text{Ta}_{1/6}\text{Nb}_{1/6}\text{Ti}_{1/6}\text{Zr}_{1/6}\text{Hf}_{1/6}\text{Mo}_{1/6})\text{C}$  and then to  $(\text{Ta}_{1/8}\text{Nb}_{1/8}\text{Ti}_{1/8}\text{Zr}_{1/8}\text{Hf}_{1/8}\text{Mo}_{1/8}\text{V}_{1/8}\text{W}_{1/8})\text{C}$ . Such a decreased tendency has been successfully reproduced in our MD simulations, demonstrating the accuracy and applicability of our training NEP in studying the thermal conductivities of HECs.

#### 4. Conclusion

In this work, we have proposed a simple and efficient strategy to construct a general NEP with wide compositional applicability for HECs, enabling accurate MD simulations on various properties. To be specific, the small 1+2HEC training dataset has been identified to be the most efficient choice to create the general NEP for HECs by systematically exploring the computational intensity and modeling complexity in DFT calculations as well as the accuracy and transferability of the trained NEPs from different datasets. A highly accurate and transferable NEP for HECs was then constructed with low RSMEs of 15.7 meV/atom, 301 meV/Å, and 49.1 meV/atom for

energy, force, and virial, respectively. Moreover, structural ( $a$ ), mechanical ( $c$ ,  $B$ , and  $G$ ), and thermal (CTEs,  $T_m$ , and thermal conductivities) properties of HECs predicted by MD simulations with our established NEP are consistent with results from DFT calculations and experimental measurements, further validating the accuracy, generalization, and reliability of our trained NEP. Our work provides a simple and efficient approach to constructing the general NEP for HECs and accelerating MD simulations on developing high-entropy ceramics with desirable properties.

## **Acknowledgments**

We acknowledge the financial support from the National Key Research and Development Program of China (No. 2021YFA0715801), the National Natural Science Foundation of China (No. 52122204), and Guangzhou Basic and Applied Basic Research Foundation (SL2023A04J00690).

## **Author Contributions**

Y. Chu conceived and designed this work. Y. Liu, H. Meng, and H. Yu performed calculations. Z. Zhu and L. Zhuang performed experiments. Y. Chu, H. Yu, and Y. Liu analyzed the data and wrote the manuscript. All authors commented on the manuscript.

## **Competing Interests**

The authors declare no competing financial interest.

## **Data Availability**

The data that support the findings of this study are available from the corresponding author upon reasonable request.

## References

- [1] C. Rost, E. Sachet, T. Borman, A. Moballegh, E. Dickey, D. Hou, J. Jones, S. Curtarolo, J. Maria, Entropy-stabilized oxides. *Nat. Commun.* 6 (2015) 8485.
- [2] J. Gild, Y. Zhang, T. Harrington, S. Jiang, T. Hu, M.C. Quinn, W.M. Mellor, N. Zhou, K. Vecchio, J. Luo, High-entropy metal diborides: A new class of high-entropy materials and a new type of ultrahigh temperature ceramics, *Sci. Rep.* 6(1) (2016) 37946.
- [3] P. Sarker, T. Harrington, C. Toher, C. Oses, M. Samiee, J.P. Maria, D.W. Brenner, K.S. Vecchio, S. Curtarolo, High-entropy high-hardness metal carbides discovered by entropy descriptors, *Nat. Commun.* 9(1) (2018) 4980.
- [4] B. Ye, T. Wen, K. Huang, C.Z. Wang, Y. Chu, First-principles study, fabrication, and characterization of  $(\text{Hf}_{0.2}\text{Zr}_{0.2}\text{Ta}_{0.2}\text{Nb}_{0.2}\text{Ti}_{0.2})\text{C}$  high-entropy ceramic, *J. Am. Ceram. Soc.* 102(7) (2019) 4344-4352.
- [5] Z. Wen, Z. Tang, Y. Liu, L. Zhuang, H. Yu, Y. Chu, Ultrastrong and high thermal insulating porous high-entropy ceramics up to 2000 °C, *Adv. Mater.* 36(14) (2024) 2311870.
- [6] X. Yan, L. Constantin, Y. Lu, J.F. Silvain, M. Nastasi, B. Cui,  $(\text{Hf}_{0.2}\text{Zr}_{0.2}\text{Ta}_{0.2}\text{Nb}_{0.2}\text{Ti}_{0.2})\text{C}$  high-entropy ceramics with low thermal conductivity, *J. Am. Ceram. Soc.* 101(10) (2018) 4486-4491.
- [7] Z. Tang, Z. Wen, Y. Liu, L. Zhuang, H. Yu, Y. Chu, Rapid experimental screening of high-entropy diborides for superior oxidation resistance, *Adv. Funct. Mater.* 34(12) (2024) 2312239.

- [8] Z. Wen, H. Meng, S. Jiang, Z. Tang, Y. Liu, Y. Chu, Non-equimolar (Hf,Zr,Ta,W) $B_2$  high-entropy diborides enable superior oxidation resistance, *Sci. China Mater.* 66(8) (2023) 3213-3222.
- [9] Z. Wen, Z. Tang, H. Meng, Y. Chu, A promising new class of high-entropy ceramics: High-entropy oxycarbides with good oxidation resistance, *Corrosion Science* 207 (2022) 110574.
- [10] Z. Wen, Z. Tang, H. Meng, L. Zhuang, H. Yu, Y. Chu, Ultrafast synthesis of high-entropy carbides up to 3,273 K for superior oxidation resistance, *Cell Rep. Phys. Sci.* 5(2) (2024) 101821.
- [11] J.X. Yang, B.H. Dai, C.Y. Chiang, I.C. Chiu, C.W. Pao, S.Y. Lu, I.Y. Tsao, S.T. Lin, C.T. Chiu, J.W. Yeh, P.C. Chang, W.H. Hung, Rapid fabrication of high-entropy ceramic nanomaterials for catalytic reactions, *ACS Nano* 15(7) (2021) 12324-12333.
- [12] B. Wang, C. Wang, X. Yu, Y. Cao, L. Gao, C. Wu, Y. Yao, Z. Lin, Z. Zou, General synthesis of high-entropy alloy and ceramic nanoparticles in nanoseconds, *Nat. Synth.* 1(2) (2022) 138-146.
- [13] J.L. Braun, C.M. Rost, M. Lim, A. Giri, D.H. Olson, G.N. Kotsonis, G. Stan, D.W. Brenner, J.P. Maria, P.E. Hopkins, Charge-induced disorder controls the thermal conductivity of entropy-stabilized oxides, *Adv. Mater.* 30(51) (2018) 1805004.
- [14] P. Zhang, Z. Lou, M. Qin, J. Xu, J. Zhu, Z. Shi, Q. Chen, M.J. Reece, H. Yan, F. Gao, High-entropy (Ca<sub>0.2</sub>Sr<sub>0.2</sub>Ba<sub>0.2</sub>La<sub>0.2</sub>Pb<sub>0.2</sub>)TiO<sub>3</sub> perovskite ceramics with A-site short-range disorder for thermoelectric applications, *J. Mater. Sci. Technol.* 97

(2022) 182-189.

- [15] D. Bérardan, S. Franger, A. Meena, N. Dragoë, Room temperature lithium superionic conductivity in high entropy oxides, *J Mater. Chem. A* 4(24) (2016) 9536-9541.
- [16] S. Chen, Z. Aitken, S. Pattamatta, Z. Wu, Z. Yu, D. Srolovitz, P. Liaw, Y. Zhang, Simultaneously enhancing the ultimate strength and ductility of high-entropy alloys via short-range ordering. *Nat. Commun.* 12 (2021) 4953
- [17] Y.F. Ye, Q. Wang, J. Lu, C.T. Liu, Y. Yang, High-entropy alloy: Challenges and prospects, *Mater. Today* 19(6) (2016) 349-362.
- [18] W. Li, S. Lyu, Y. Chen, A.H.W. Ngan, Fluctuations in local shear-fault energy produce unique and dominating strengthening in metastable complex concentrated alloys, *Proc. Natl. Acad. Sci. U.S.A.* 120(12) (2023) e2209188120.
- [19] Y. Mishin, Machine-learning interatomic potentials for materials science, *Acta Mater.* 214 (2021) 116980.
- [20] J. Behler, Perspective: Machine learning potentials for atomistic simulations, *J. Chem. Phys.* 145(17) (2016) 170901.
- [21] Y. Zuo, C. Chen, X. Li, Z. Deng, Y. Chen, J. Behler, G. Csányi, A.V. Shapeev, A.P. Thompson, M.A. Wood, S.P. Ong, Performance and cost assessment of machine learning interatomic potentials, *J. Phys. Chem. A* 124(4) (2020) 731-745.
- [22] Z. Zeng, F. Wodaczek, K. Liu, F. Stein, J. Hutter, J. Chen, B. Cheng, Mechanistic insight on water dissociation on pristine low-index TiO<sub>2</sub> surfaces from machine learning molecular dynamics simulations, *Nat. Commun.* 14(1) (2023) 6131.

- [23] M. Liu, J. Wang, J. Hu, P. Liu, H. Niu, X. Yan, J. Li, H. Yan, B. Yang, Y. Sun, C. Chen, G. Kresse, L. Zuo, X.Q. Chen, Layer-by-layer phase transformation in  $\text{Ti}_3\text{O}_5$  revealed by machine-learning molecular dynamics simulations, *Nat. Commun.* 15(1) (2024) 3079.
- [24] S. Lin, L. Casillas-Trujillo, F. Tasnádi, L. Hultman, P.H. Mayrhofer, D.G. Sangiovanni, N. Koutná, Machine-learning potentials for nanoscale simulations of tensile deformation and fracture in ceramics, *npj Comput. Mater.* 10(1) (2024) 67.
- [25] F.Z. Dai, Y. Sun, B. Wen, H. Xiang, Y. Zhou, Temperature dependent thermal and elastic properties of high entropy  $(\text{Ti}_{0.2}\text{Zr}_{0.2}\text{Hf}_{0.2}\text{Nb}_{0.2}\text{Ta}_{0.2})\text{B}_2$ : Molecular dynamics simulation by deep learning potential, *J. Mater. Sci. Technol.* 72 (2021) 8-15.
- [26] F.Z. Dai, B. Wen, Y. Sun, H. Xiang, Y. Zhou, Theoretical prediction on thermal and mechanical properties of high entropy  $(\text{Zr}_{0.2}\text{Hf}_{0.2}\text{Ti}_{0.2}\text{Nb}_{0.2}\text{Ta}_{0.2})\text{C}$  by deep learning potential, *J. Mater. Sci. Technol.* 43 (2020) 168-174.
- [27] V. Choyal, N. Sagar, G. Gautam, Constructing and evaluating machine-learned interatomic potentials for Li-based disordered rocksalts, *J. Chem. Theory Comput.* 20(11) (2024) 4844-4856.
- [28] K. Song, R. Zhao, J. Liu, Y. Wang, E. Lindgren, Y. Wang, S. Chen, K. Xu, T. Liang, P. Ying, General-purpose machine-learned potential for 16 elemental metals and their alloys, arXiv preprint arXiv:2311.04732 (2023).
- [29] G. Kresse, J. Furthmüller, Efficiency of ab-initio total energy calculations for metals and semiconductors using a plane-wave basis set, *Comput. Mater. Sci.* 6(1)

- (1996) 15-50.
- [30] P.E. Blöchl, Projector augmented-wave method, *Phys. Rev. B* 50(24) (1994) 17953-17979.
- [31] J.P. Perdew, K. Burke, M. Ernzerhof, Generalized gradient approximation made simple, *Phys. Rev. Lett.* 77(18) (1996) 3865-3868.
- [32] A. Zunger, S.H. Wei, L.G. Ferreira, J.E. Bernard, Special quasirandom structures, *Phys. Rev. Lett.* 65(3) (1990) 353-356.
- [33] A. van de Walle, Multicomponent multisublattice alloys, nonconfigurational entropy and other additions to the Alloy Theoretic Automated Toolkit, *Calphad* 33(2) (2009) 266-278.
- [34] V. Wang, N. Xu, J.C. Liu, G. Tang, W.T. Geng, VASPKIT: A user-friendly interface facilitating high-throughput computing and analysis using VASP code, *Comput. Phys. Commun.* 267 (2021) 108033.
- [35] R. Hill, The elastic behaviour of a crystalline aggregate, *Proc. Phys. Soc. A* 65(5) (1952) 349.
- [36] R. Jinnouchi, J. Lahnsteiner, F. Karsai, G. Kresse, M. Bokdam, Phase transitions of hybrid perovskites simulated by machine-learning force fields trained on the fly with bayesian inference, *Phys. Rev. Lett.* 122(22) (2019) 225701.
- [37] H.J. Monkhorst, J.D. Pack, Special points for Brillouin-zone integrations, *Phys. Rev. B* 13(12) (1976) 5188-5192.
- [38] Z. Fan, Y. Wang, P. Ying, K. Song, J. Wang, Y. Wang, Z. Zeng, K. Xu, E. Lindgren, J.M. Rahm, A.J. Gabourie, J. Liu, H. Dong, J. Wu, Y. Chen, Z. Zhong, J. Sun, P.

- Erhart, Y. Su, T. Ala-Nissila, GPUMD: A package for constructing accurate machine-learned potentials and performing highly efficient atomistic simulations, *J. Chem. Phys.* 157(11) (2022).
- [39] A.P. Thompson, H.M. Aktulga, R. Berger, D.S. Bolintineanu, W.M. Brown, P.S. Crozier, P.J. in 't Veld, A. Kohlmeyer, S.G. Moore, T.D. Nguyen, R. Shan, M.J. Stevens, J. Tranchida, C. Trott, S.J. Plimpton, LAMMPS - a flexible simulation tool for particle-based materials modeling at the atomic, meso, and continuum scales, *Comput. Phys. Commun.* 271 (2022) 108171.
- [40] Y. Liu, Z. Zhu, Z. Tang, H. Yu, L. Zhuang, Y. Chu, Unraveling lattice-distortion hardening mechanisms in high-entropy carbides, *Small* (2024), <https://doi.org/10.1002/sml.202403159>.
- [41] M.C. Roufosse, P.G. Klemens, Thermal conductivity of complex dielectric crystals, *Phys. Rev. B* 7 (1973) 5379-5386.
- [42] F. Wang, X. Yan, T. Wang, Y. Wu, L. Shao, M. Nastasi, Y. Lu, B. Cui, Irradiation damage in  $(\text{Zr}_{0.25}\text{Ta}_{0.25}\text{Nb}_{0.25}\text{Ti}_{0.25})\text{C}$  high-entropy carbide ceramics, *Acta Mater.* 195 (2020) 739-749.
- [43] J. Dusza, P. Švec, V. Girman, R. Sedlák, E.G. Castle, T. Csanádi, A. Kovalčíková, M.J. Reece, Microstructure of  $(\text{Hf-Ta-Zr-Nb})\text{C}$  high-entropy carbide at micro and nano/atomic level, *J. Eur. Ceram. Soc.* 38(12) (2018) 4303-4307.
- [44] Z. Li, Z. Wang, Z. Wu, B. Xu, S. Zhao, W. Zhang, N. Lin, Phase, microstructure and related mechanical properties of a series of  $(\text{NbTaZr})\text{C}$ -Based high entropy ceramics, *Ceram. Int.* 47(10) (2021) 14341-14347.

- [45] V. K. R. Gorle, A. S. S.R. Bakshi, Novel single phase  $(\text{Ti}_{0.2}\text{W}_{0.2}\text{Ta}_{0.2}\text{Mo}_{0.2}\text{V}_{0.2})\text{C}_{0.8}$  high entropy carbide using ball milling followed by reactive spark plasma sintering, *J. Eur. Ceram. Soc.* 41(13) (2021) 6756-6762.
- [46] Y.-J. Wang, H.-J. Li, Q.-G. Fu, H. Wu, D.-J. Yao, B.-B. Wei, Ablative property of HfC-based multilayer coating for C/C composites under oxy-acetylene torch, *Appl. Surf. Sci.* 257(10) (2011) 4760-4763.
- [47] B. Zhang, J. Yin, Y. Wang, D. Yu, H. Liu, X. Liu, M.J. Reece, Z. Huang, Low temperature densification mechanism and properties of  $\text{Ta}_{1-x}\text{Hf}_x\text{C}$  solid solutions with decarbonization and phase transition of  $\text{Cr}_3\text{C}_2$ , *J. Materiomics* 7(4) (2021) 672-682.
- [48] Y.S. Touloukian, R.K. Kirby, E.R.M. Taylor, T.Y.R. Lee, Thermophysical properties of matter. volume 13 thermal expansion - nonmetallic Solids, IFI/Plenum Data Company, New York, 1977.
- [49] J.H. Richardson, Thermal expansion of three group IVA carbides to 2700 °C, *J. Am. Ceram. Soc.* 48(10) (1965) 497-499.
- [50] R. Riedel, Handbook of ceramic hard materials, Wiley-VCH, 2000.
- [51] R.O. Elliott, C.P. Kempter, Thermal expansion of some transition metal carbides, *J. Phys. Chem.* 62(5) (1958) 630-631.
- [52] D.G. Sangiovanni, F. Tasnádi, T. Harrington, M. Odén, K.S. Vecchio, I.A. Abrikosov, Temperature-dependent elastic properties of binary and multicomponent high-entropy refractory carbides, *Mater. Des.* 204 (2021) 109634.
- [53] B.A. Mathe, Surface Brillouin scattering studies of elastic properties of materials

at high temperature, thesis, 2008.

- [54] A. Krajewski, L. D'Alessio, G. De Maria, Physico-chemical and thermophysical properties of cubic binary carbides, *Cryst. Res. Technol.* 33(3) (1998) 341-374.
- [55] R.O. Elliott, C.P. Kempter, Thermal expansion of some transition metal carbides, *J. Phys. Chem. A* 62 (1958) 630-631.
- [56] R.O. Elliott, C.P. Kempter, Thermal expansion of some transition metal carbides, *J. Phys. Chem.* 62 (1958) 630-631.
- [57] A. Jain, S.P. Ong, G. Hautier, W. Chen, W.D. Richards, S. Dacek, S. Cholia, D. Gunter, D. Skinner, G. Ceder, K.A. Persson, Commentary: The Materials Project: A materials genome approach to accelerating materials innovation, *APL Mater.* 1(1) (2013).
- [58] H. Meng, R. Yu, Z. Tang, Z. Wen, Y. Chu, Formation ability descriptors for high-entropy carbides established through high-throughput methods and machine learning, *Cell Rep. Phys. Sci.* 4(8) (2023) 101512.
- [59] O. Cedillos-Barraza, D. Manara, K. Boboridis, T. Watkins, S. Grasso, D.D. Jayaseelan, R.J.M. Konings, M.J. Reece, W.E. Lee, Investigating the highest melting temperature materials: A laser melting study of the TaC-HfC system, *Sci. Rep.* 6(1) (2016) 37962.
- [60] D.L. Perry, *Handbook of inorganic compounds*, CRC Press, 2016.
- [61] M.G.D.V. Cuppari, S.F. Santos, Physical properties of the NbC carbide, *Metals* 6(10) (2016) 250.
- [62] M. Baucio, *ASM engineering materials reference book*, 2nd ed., ASM

International, 1994.

## Supporting Information

# **An efficient strategy to construct general machine learning potentials for high-entropy ceramics**

Yiwen Liu, Hong Meng, Zijie Zhu, Hulei Yu\*, Lei Zhuang, Yanhui Chu\*

School of Materials Science and Engineering, South China University of Technology,

Guangzhou, 510641, China

---

\* Corresponding author.

*E-mail address:* [huleiyu@scut.edu.cn](mailto:huleiyu@scut.edu.cn) (H. Yu); [chuyh@scut.edu.cn](mailto:chuyh@scut.edu.cn) (Y. Chu)

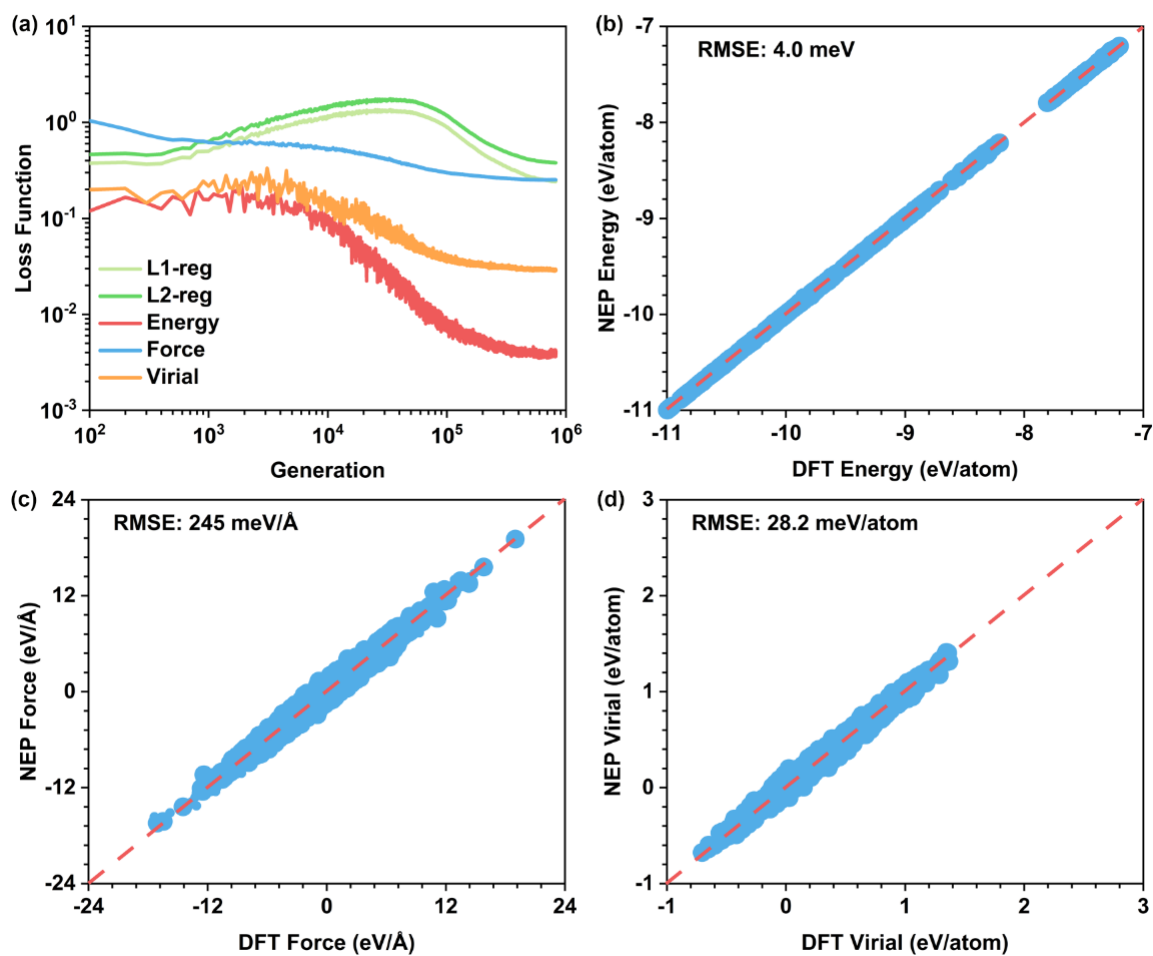


**Figure S1** Performance of the constructed NEP based on the small-scale 1HEC training dataset.

(a) Evolution of various loss functions with respect to generations. (b) Energy, (c) force, and (d) virial from NEP and DFT calculations for the 1HEC training dataset.

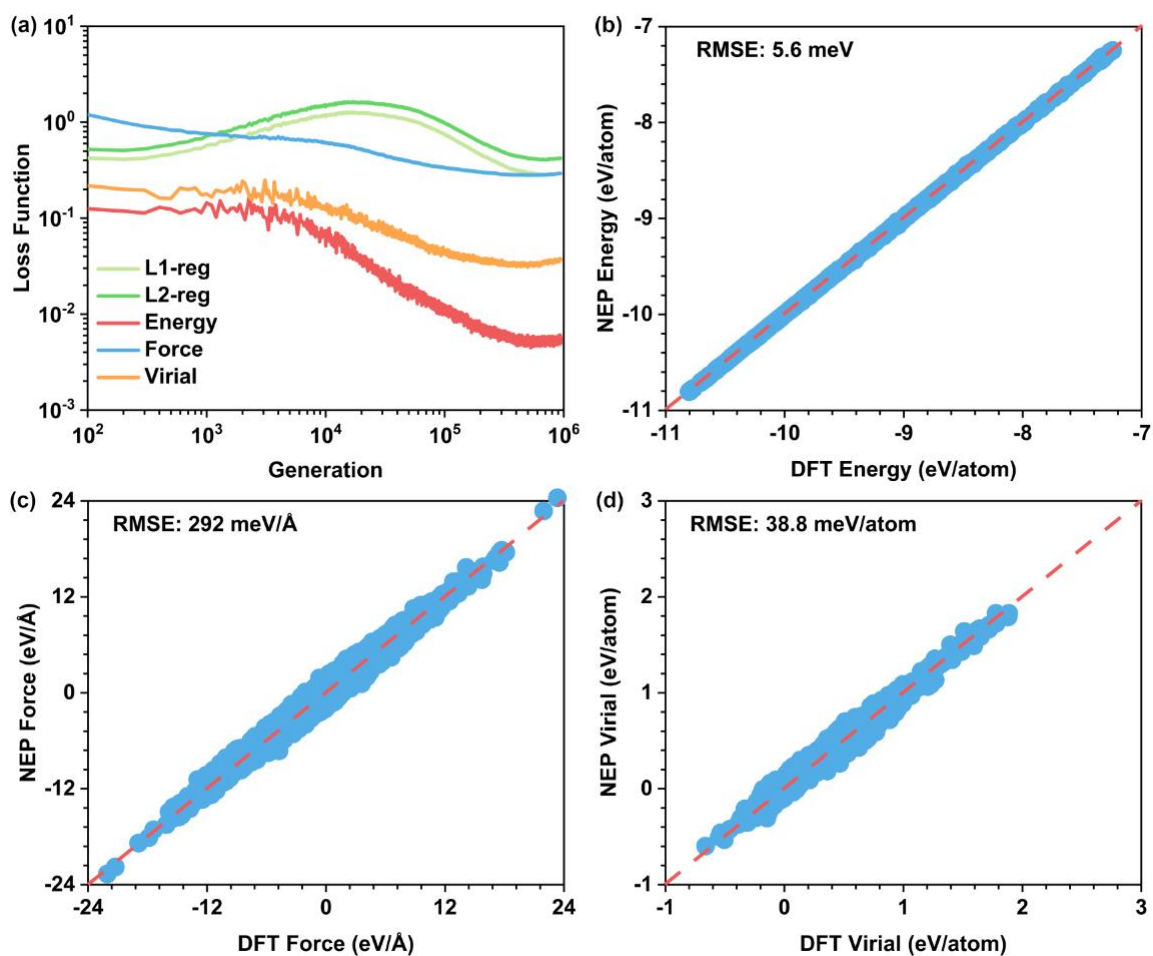


**Figure S2** Performance of the constructed NEP based on the small-scale 2HEC training dataset.

(a) Evolution of various loss functions with respect to generations. (b) Energy, (c) force, and (d) virial from NEP and DFT calculations for the 2HEC training dataset.

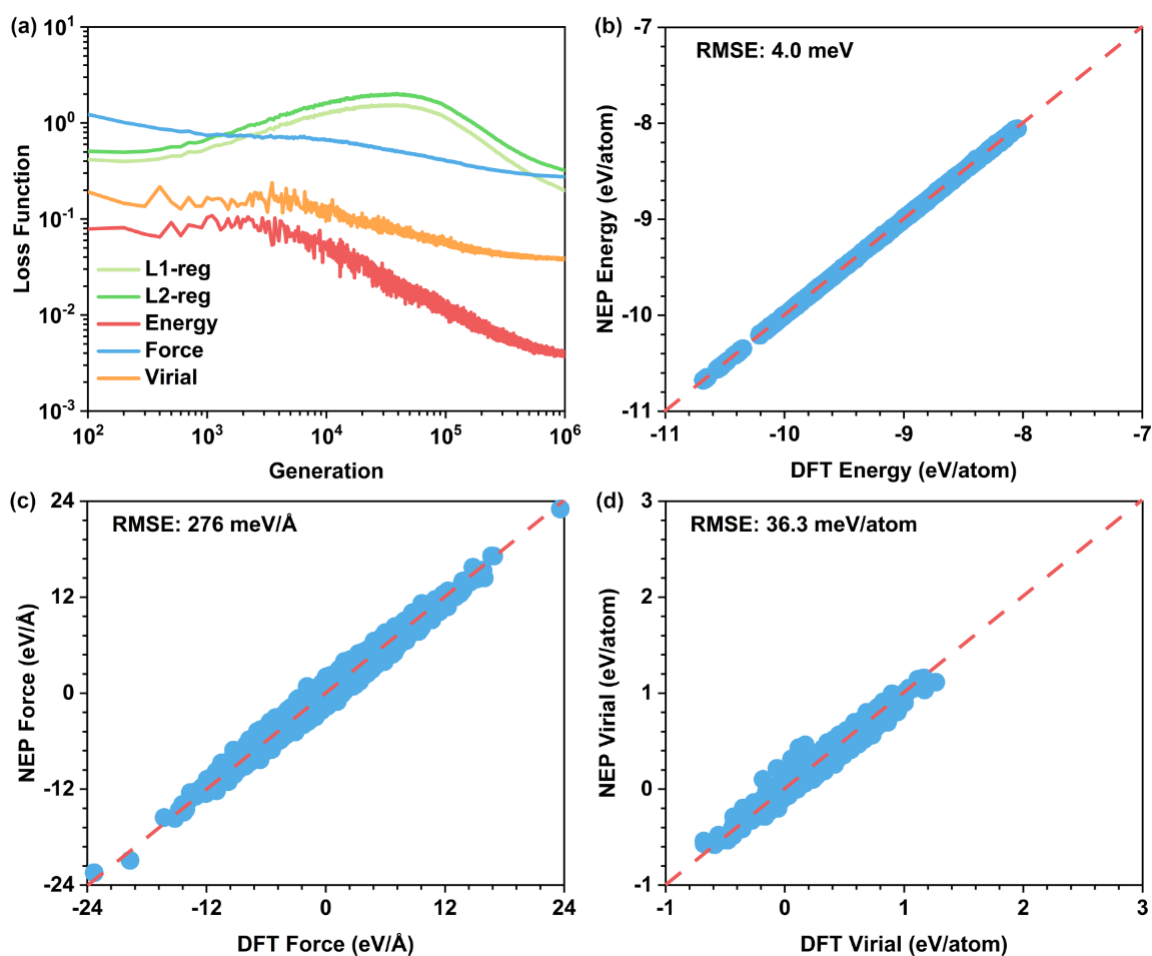


**Figure S3** Performance of the constructed NEP based on the small-scale 3HEC training dataset.

(a) Evolution of various loss functions with respect to generations. (b) Energy, (c) force, and (d) virial from NEP and DFT calculations for the 3HEC training dataset.

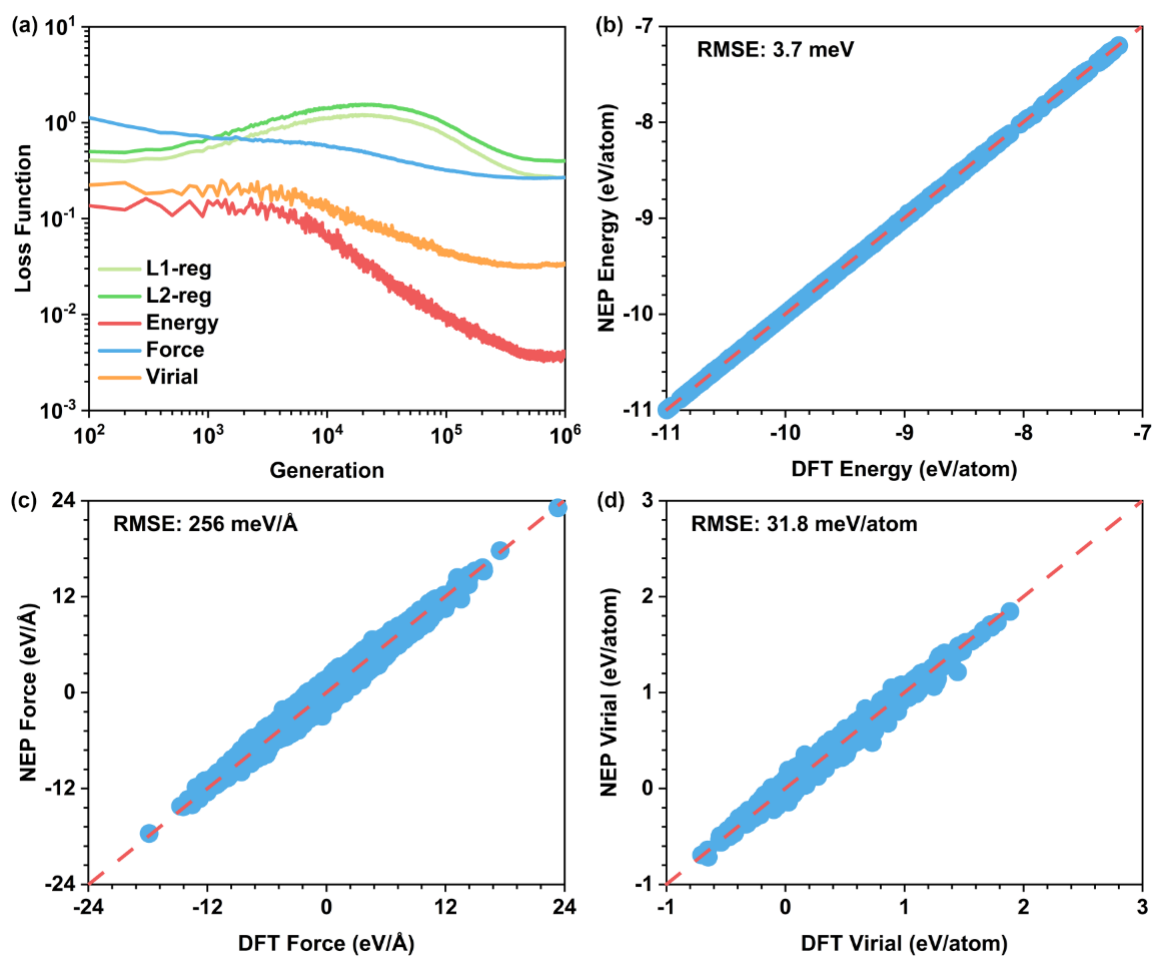


**Figure S4** Performance of the constructed NEP based on the small-scale 1+2HEC training dataset. (a) Evolution of various loss functions with respect to generations. (b) Energy, (c) force, and (d) virial from NEP and DFT calculations for the 1+2HEC training dataset.

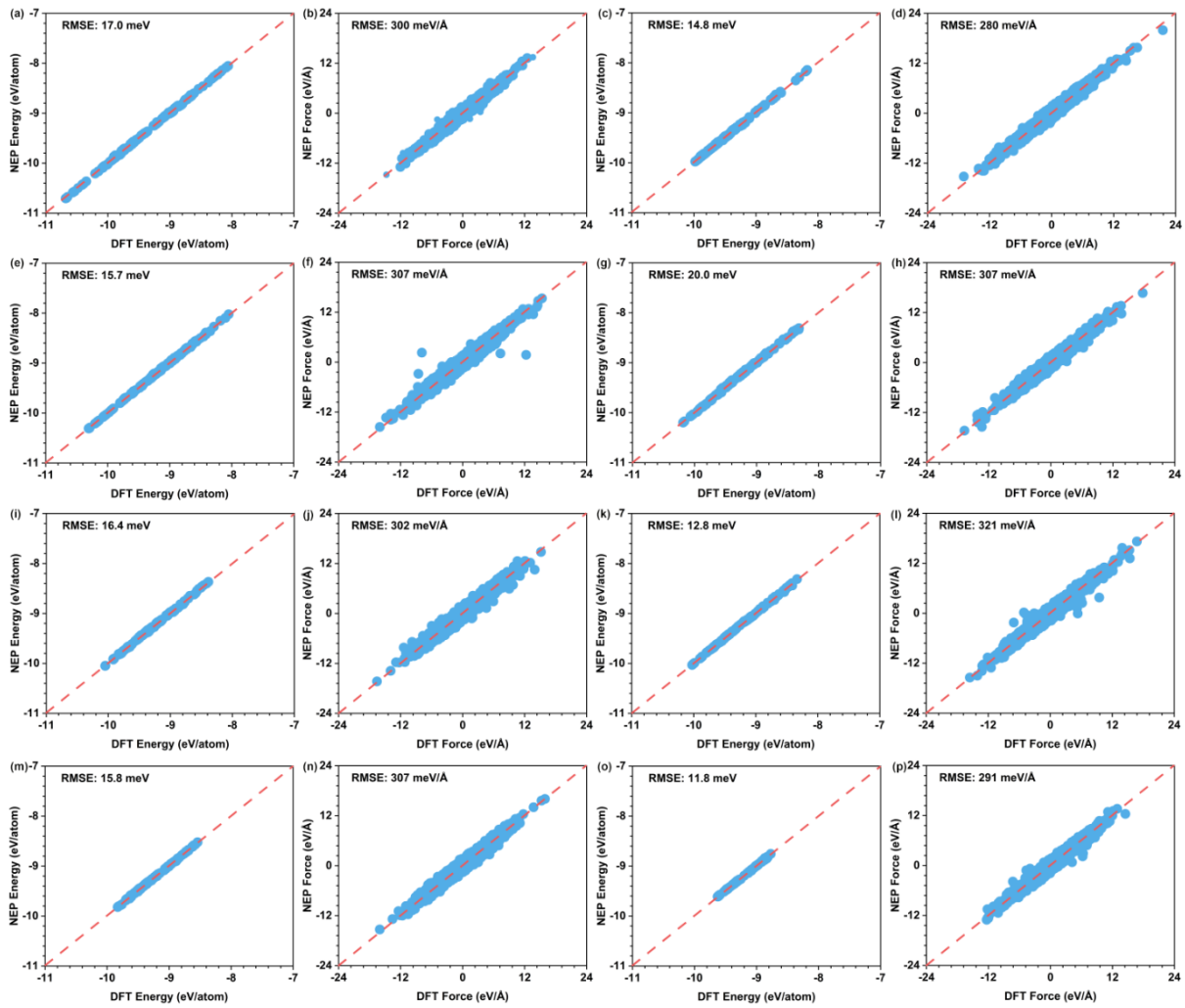


**Figure S5** Performance of the constructed NEP based on large-scale 1+2HEC training dataset.

(a, c, e, g, i, k, m, o) Energy and (b, d, f, h, j, l, n, p) force from NEP and DFT calculations for  $n$ HEC ( $n = 3-10$ ) testing datasets, respectively.

**Table S1** The supercells for 1-10HECs.

Compounds	Supercells
1HEC	2×2×4
2HEC	2×2×4
3HEC	2×3×3
4HEC	2×2×4
5HEC	2×2×5
6HEC	2×3×3
7HEC	2×2×7
8HEC	2×2×4
9HEC	3×3×3
10HEC	2×2×5

**Table S2** The NEP training hyperparameters.

Keywords	Parameters	Parameter setting description
version	4	neuroevolution potential version
type	Zr, Ti, Nb, Ta, Hf, Mo, V, W, Sc, Y,	list of chemical element types
	C	
cutoff	8, 4	radial and angular cutoffs
$n_{\max}$	4, 4	size of the radial and angular basis
basis <sub>size</sub>	12, 12	number of radial angular basis functions
$l_{\max}$	4, 2	expansion order for angular terms
neuron	50	number of neurons
$\lambda_e$	1	weight of energy loss term
$\lambda_f$	1	weight of force loss term
$\lambda_v$	0.2	weight of virial loss term
batch	200	batch size for training
population	50	population size
generation	1000000	number of generations

**Table S3** Melting points of carbides from NEP calculations and reported experiments, as well as their difference ( $\Delta$ ).

Carbides	HfC	TaC	ZrC	NbC	TiC	VC
Cal (K)	4082	3860	3680	3600	3500	3317
Exp (K)	4232 [1]	4041 [1]	3813 [2]	3873 [3]	3430 [4]	3080 [2]
$\Delta$ (%)	3.54	4.48	3.49	7.05	-2.04	-7.69

## References

- [1] O. Cedillos-Barraza, D. Manara, K. Boboridis, T. Watkins, S. Grasso, D.D. Jayaseelan, R.J.M. Konings, M.J. Reece, W.E. Lee, Investigating the highest melting temperature materials: A laser melting study of the TaC-HfC system, *Sci. Rep.* 6(1) (2016) 37962.
- [2] D.L. Perry, *Handbook of inorganic compounds*, CRC Press, 2016.
- [3] M.G.D.V. Cuppari, S.F. Santos, Physical properties of the NbC carbide, *Metals* 6(10) (2016) 250.
- [4] M. Baucio, *ASM engineering materials reference book*, 2nd ed., ASM International, 1994.